Experimental and Numerical Studies on Failure Behaviours of Sandstones Subject to Freeze-Thaw Cycles

Javad Yahaghi [1], Hongyuan Liu [1*], Andrew Chan [1] and Daisuke Fukuda [1,2]

[1] School of Engineering, University of Tasmania, Hobart, TAS 7001, Australia

[2] Faculty of Engineering, Hokkaido University, Hokkaido 060-8628, Japan

Abstract

The freeze-thaw induced damage of rock affects the durability and serviceability of geo-structures, especially those constructed in the regions frequently impacted by climatic changes. A series of laboratory tests including P-wave velocity tests, freeze-thaw tests, uniaxial compression strength (UCS) tests and Brazilian tensile strength (BTS) tests are conducted to investigate the physical-mechanical properties and failure behaviours of Tasmanian sandstones subjected to various freeze-thaw cycles. It is observed that the P-wave velocity, BTS and UCS of the sandstone decrease as the number of freeze-thaw cycles increases, in which the decreasing rate from 0 to 20 freeze-thaw cycles was more pronounced than that from 20 to 40 and 40 to 60 freeze-thaw cycles. Moreover, it is found that the main failure mode of the sandstone changes from axial splitting to shearing along a single plane in the UCS tests and from central smooth fractures to a central zigzag fracture in the BTS tests with the number of freeze-thaw cycles increasing. Three-dimensional (3D) numerical modellings are then conducted using a self-developed 3D hybrid finite-discrete element method (HFDEM) parallelized on the basis of general-purpose graphic processing units (GPGPU) to further investigate the failure mechanisms of Tasmanian sandstones subjected to various freeze-thaw cycles in the UCS and BTS tests. The 3D numerical modellings agree very well with the experimental observations that the physical-mechanical parameters of the sandstone degrade with the increasing number of the freeze-thaw cycles. Moreover, the 3D numerical modellings reveal the deterioration and failure mechanisms of sandstones subjected to various freeze-thaw cycles. For the sandstone specimens without subjecting to freeze-thaw cycles, axial splitting is the main failure pattern while tensile and mixed-mode damages are the dominant failure mechanism in the UCS tests. For the sandstone subjecting to various freeze-thaw cycles, the increasing number of freeze-thaw cycles causes the macroscopic cracks to propagate, interact and coalesce in the shear behaviour resulting in the final shear fracture pattern in the UCS test. The 3D numerical modellings of the BTS test show that, although, for both the models with and without subjecting to freezing and thawing cycles, a central fracture is the eventual failure pattern, the failure surface becomes more zigzag as the number of freeze-thaw cycles increases.

[*] Corresponding author: Dr Hongyuan Liu (Email: Hong.Liu@utas.edu.au and Tel: 0061 6226 2113):

Keywords: Freeze-thaw cycles, rock, sandstone, UCS, BTS, 3D fracture process analysis and FDEM

1. Introduction

Rock is one of the most common natural construction materials on Earth. Cold regions, including permafrost areas and seasonally freezing areas, constitute a large portion of Earth's continent. More than 20% of the continental surface in the northern hemisphere are occupied by permafrost, whereas more than half of the surface experiences seasonal freezing and thawing [1]. In the southern hemisphere, Antarctica is known as the coldest continent on the Earth. In most coastal regions of Antarctica, the mean annual temperature is around -12°C while the lowest surface temperature ever recorded is -89°C at Russian Vostok station within Australian Antarctic Territory [2]. Tasmania has a generally cooler and wetter climate than that in other states of Australia. The temperature of Tasmania in winter can go as low as -14 °C in the highlands such as Central Plateau although the coastal areas rarely go below freezing and the summer temperatures can reach up to 41°C. While increasing human economic activities have led to the construction of more and more geotechnical engineering structures in cold regions, it is expected that, in the future, more infrastructures will be constructed in southern hemisphere.

Any kind of natural rocks and geo-structures in these cold regions are not only subjected to external loads but also experiencing severe environmental effects. Freeze and thaw induced settlement is a common phenomenon observed in seasonal freezing areas and is the cause of significant damage to the built infrastructure [3], [4]. As an example, an uplifting displacement of 88 mm has been caused by the freeze and thaw cycles and has led to the deformations and crackings of the supporting concrete structure of the centre columns of the Myllypuro Ice Rink facility in Finland [3]. Long-term monitoring of average global temperatures indicate an ongoing change of the climate [5], which has resulted increasing temperatures in permafrost. The increasing temperature leads to thawing of portions of the permafrost area and thickening of the upper crust layer where the active freezing-thawing cycles occur, which then result in considerable settlement of the ground surface damaging infrastructures. Therefore, understanding the behaviour of rock upon the freezing and thawing cycles is essential to adapt the operation practices, design philosophies and develop suitable methods to minimize the damages [6].

One of the earliest documented cases of investigating the behaviour of grounds subjected to the freezing and thawing cycles was the use of artificial freezing at Brunkeberg tunnel in Stockholm in 1876 [7]. As the industrial development was accelerating in northern Russia to

develop railways and mining operations in the late nineteenth century, the study of permafrost as an applied science began to protect civil structures from freeze-thaw damages [1]. The deterioration of rock under frost-heave and freeze-thaw cycles has become an unavoidable concern in engineering such as road, railroad, bridge, tunnelling, pipeline, and building constructions [8]–[10].

The deterioration of rock under freeze-thaw actions has been investigated by many researchers through relating one or more physical-mechanical properties of rocks such as moisture content, mineralogical composition, texture, rock strength, and pore microstructure to single factor of freeze-thaw actions such as temperature range, frequency and applied stress. However, the freeze-thaw action and loading are both repetitive cycles and the joint action may worsen the damage of rock and lead to severe deterioration of the long-term mechanical properties of rock. Tan et al. [10] found that the elastic modulus, compressive strength and cohesive strength of biotite granite decreased significantly with the number of freeze-thaw cycles increasing. A statistical model was developed by Bayram [11] to estimate the UCS of limestones after subjecting to freeze-thaw cycles. Another statistical model was proposed to experimentally investigate various rock index properties, including the dry density, ultrasonic velocity, point load strength, and slake-durability test indexes, after freeze-thaw cycles [12]. Wang et al. [13] investigated the physical properties of sandstone specimens subjected to freeze-thaw cycles, including the density, porosity, P-wave velocity, UCS, and deformation modulus. Various researchers have extensively studied the mechanical behaviours of transversely isotropic rocks such as slate subjected to freeze-thaw cycles and developed some corresponding models [14]–[21]. Moreover, another study [22] conducted triaxial compression tests with various confining pressures of 5, 10 and 20 MPa to investigate the change of wave velocities, mechanical properties and permeability characteristics of red sandstone. The specimens were divided into four groups, and underwent 0, 4, 8 and 12 freezing and thawing cycles. It was found that the increase of the numbers of freeze-thaw cycles decreased the UCS, elastic modulus, cohesion, angle of internal friction and P-wave velocity of the red sandstone. It was concluded that the damage of rock caused by the freeze-thaw cycles led to the changes of microstructure and then mechanical performance. Ultrasonic and mechanical tests including compression, tension and shear, of red sandstones subjected to freeze-thaw cycles were carried out in another study, which concluded that the red sandstone performed worse as the numbers of freeze-thaw cycles increased [23]. Generally the rock with a lower porosity has a higher strength so that a greater suction force (hence, a lower temperature) is required for the low porosity rocks to crack [24]

during the freeze-thaw tests. According to Matsuoka [24], high porosity rocks begin to crack at 0 to -1 °C and terminate at about -5 °C in the freeze-thaw tests, while in medium porosity rocks the cracking temperature is between -3 °C and -6 °C and in low porosity rocks the cracking starts below -4 °C.

To summarize the findings above, although many researches have been conducted based on laboratory tests to investigate the effect of freeze-thaw cycles and have shown a decrease of the mechanical properties of the rocks with the freeze-thaw cycles increasing, there is no consensus on the effects of the specific number of freeze-thaw cycles, freezing temperature and combination of freeze-thaw cycles with loads on the deterioration of rock subjected to various number of freeze-thaw cycles.

In order to gain a further understanding of the effect of freeze-thaw cycles on the rock deterioration and failure, some scholars have implemented numerical methods to analyse the freeze-thaw induced damage besides the experimental methods. A simple linear stress-strain constitutive relationship was implemented into a two-dimensional (2D) plane strain finite element model with a thermal-mechanical-flow coupling to simulate freeze-thaw experiments [25]. An isogeometric analysis-based numerical model was applied to simulate the thermo-hydromechanically coupled processes in ground freezing [26]. Another research conducted numerical analyses to investigate the stability of a rock mass slope subjected to freeze-thaw cycles [27], in which the freeze-thaw coefficient of the rock was firstly measured and the generalized Hoek-Brown criterion was then employed to determine the parameters of slope rock mass stablishing a numerical rock slope excavation model. According to another numerical study, the volume expansion from the freeze-thaw cycles applied an stable force on joints which resulted in the tensile stress concentration area emerging at the joint tip [28]. In another research [29], the variations of the modal parameters such as resonant frequencies, damping ratios and mode shapes were analysed to assess the freeze-thaw resistance of limestone through a finite element model.

These numerical studies greatly increased our understanding of the effect of freeze-thaw cycles on the physical-mechanical behaviour of rocks. However, most of those numerical modellings are conducted in two-dimension (2D). Three-dimensional (3D) modelling is seldom conducted to investigate the effect of freeze-thaw cycles on the deterioration of the physical-mechanical parameters and failure progressive process although 3D modellings of rock failure process under mechanical loads using various numerical methods have been conducted in literatures

[30], [31], [32], [33]. Moreover, although complex thermo-mechanical-hydro coupling modelling or even 3D modelling have been conducted using finite element methods (FEM) in several literatures, the fracture behaviour of rocks is not modelled due to the limitation of continuum mechanics – based FEM in dealing with rock fracture and fragmentation. Besides, there is a lack of research on the effect of freeze-thaw cycles on the deterioration of rocks in Australia or even southern Hemisphere. Therefore, further research is necessary to investigate the fracture mechanism of rock under freeze-thaw cycles using advanced numerical methods which are capable of modelling rock fracture.

Correspondingly, the main aim of the present work is to experimentally investigate the physical-mechanical and failure behaviours of Tasmanian sandstones subjected to the freezing and thawing cycles and then numerically simulate them using a self-developed 3D hybrid finite-discrete element method (HFDEM), which is parallelized on the basis of general purpose graphic processing units (GPGPU) and capable of modelling rock fracture and fragmentation [34]–[36].

The remaining part of this paper is organized as follows; both the experimental testing method and numerical method are firstly presented. The deterioration of the physical-mechanical properties of the sandstone subjected to various freeze-thaw cycles are then quantified using the experimental testing method and discussed on the basis of damage mechanics, which justifies that the freeze-thaw induced damage can be modelled by deteriorating the physical-mechanical parameters of rocks with the number of freeze-thaw cycle increasing. After that, a GPGPU-parallelized HFDEM is implemented to model the damaging mechanism and failure progressive process of the sandstone subjected to various freeze-thaw cycles in the uniaxial compression strength (UCS) tests and Brazilian tensile strength (BTS) tests. Finally, the results from the experimental tests and numerical simulations are compared with each other to conclude the deterioration and failure mechanism and the fracture patterns of the sandstones subjected to various freeze-thaw cycles.

2. Research Methods

2.1. Experimental tests

The target sandstone cores were obtained through diamond drilling with the drill size of HQTT from the construction site of the Museum of Old and New Art (MONA 42.8125° S, 147.2615° E) located on the Berriedale peninsula in Tasmania, Australia. The diamond drilling was conducted perpendicularly to the bedding plane and the sandstone specimen was then cut

perpendicularly to the axis of the drill cores, i.e. parallelly to the bedding plane but the specimens around the bedding plane were dropped to avoid any obvious heterogeneities. Each sandstone specimen for the UCS test had a diameter of 60 mm and a height of 165 mm while that for the BTS test had a diameter of 60 mm and a height of 30 mm. Thus, the height to diameter ratios of the rock specimens were 2.75 and 0.5 for the UCS and BTS tests, respectively, and the sizes of the specimens met the requirements of ISRM for both UCS and BTS tests [37]. Before any UCS or BTS tests, P-wave velocities of all the rock specimens were measured using a Pundit PL-200 testing equipment from Proceq, as shown in Fig. 1.

After that, the rock specimens were divided into 4 sets with 6 specimens in each set (three for UCS and another there for BTS). One set of specimens were directly subjected to the UCS and BTS tests. This set corresponded to the reference case of zero freeze-thaw cycle. For other 3 sets of specimens, before either UCS or BTS tests were conducted, the specimens were firstly immersed in the pure water for two weeks and then put into a climatic cabinet for freeze-thaw tests. A climatic controlled cabinet with an environmental chamber controller (Fig. 2. i)) was employed for the freeze-thaw tests, during which the conditions of the climatic cabinet, i.e. temperatures and moistures were set following those in previous researches [22], [38]–[40] and corresponding to the climatic conditions in Tasmania. As can be seen from Fig. 2. ii), one cycle consisted of 9 hours of freezing time (which included 1 hour for reducing the temperature from +20 to −20 °C and 8 hours at the constant of -20 °C) and 9 hours of thawing time (which included 1 hour for increasing the temperature from -20 to +20 °C and 8 hours at the constant of +20 °C), which were efficient for the heat transfer and uniform temperature distribution during each phase according to previous researches [22], [38]–[40]. During the switch between the freeze-thaw cycles, the temperature varied between +20 °C to -20 °C by the changing rate of 0.67 °C/min. The humidity in the climatic cabinet was kept 100%, which made sure that the specimens would not lose any moistures although they were not sealed. The number of freeze-thaw cycles for three sets of the rock specimens was set as 20, 40 and 60.

After the freeze-thaw tests, the P-wave velocities of cylindrical sandstone specimens along their axial directions were measured again under the room temperature +20 °C. Finally, the UCS and BTS tests were conducted for all the specimens in each set using a Matest high stability compression testing apparatus with an automatic servo-controlled system (Fig. 3) by following the ISRM standards. The testing system includes a hydraulic loading system with the capacity of 2000 kN, an electronic measurement system and a data acquisition and processing UTMII software which records all testing data in a USB disc drive.

2.2. Numerical methods and models

2.2.1 Introduction to the numerical method of GPGPU-parallelized HFDEM

GPGPU-parallelized HFDEM is to be implemented to model the damaging mechanism and failure progressive process of the sandstones subjected to various freeze-thaw cycles in the UCS and BTS tests. It is a hybrid finite-discrete element method (HFDEM) developed by the authors [41] on the basis of the open source Y library [42] and further parallelized by the authors on the basis of general-purpose graphic processing units (GPGPU) [36]. The GPGPU-parallelized HFDEM has passed a series of fundamental rock mechanics tests [41], [43] and provides a powerful numerical tool to investigate the fracture and fragmentation of rocks under various static and dynamic loading conditions. Compared with the numerical methods reviewed in the introduction section, GPGPU-parallelized HFDEM can naturally model the damage and cracking behaviour of rocks induced by the freeze-thaw cycles and the fracture and fragmentation of rocks in the UCS and BTS tests through its damaging and fracturing algorithm, i.e. transition from continuum to discontinuum, which is explained in next paragraph since a complete introduction of GPGPU-parallelized HFDEM can be found in the authors' former publications [36], [41].

In GPGPU-parallelized HFDEM, rocks are modelled in 3D and discretized into an assembly of tetrahedral finite elements in the same way as that in the traditional FEM. Different from the traditional FEM, initially zero-thickness cohesive elements are inserted between any adjacent finite elements, which may damage and then completely break to allow open and/or slide to occur depending on local loading conditions there. The damage of the cohesive elements follows the concept of a smeared crack [35], [44], as shown in Fig. 4. Once the Mohr-Coulomb strength criterion with tension cut-off is satisfied, the cohesive element damages in either tensile or shear modes, i.e. mode-I or mode-II, following the tensile or shear softening curves shown in Fig. 4. i) and ii), respectively. The corresponding mode-I and mode-II damage variables are defined as $D_I = (o - o_p)/o_t$ and $D_{II} = (s - s_p)/s_t$, respectively, where o and s are the opening and sliding displacements, respectively, o_p and s_p are the elastic limits of the opening and sliding displacements, and o_t and s_t are the ultimate limits of the opening and sliding displacements. The mixed-mode damage variable is defined as $D_{Mixed} = min\left(1, \sqrt{D_I^2 + D_{II}^2}\right)$.

2.2.2 Numerical models

The modelled cylindrical specimens have a size of 60 mm in diameter and 165 mm in height in the UCS test (Fig. 5. i)) and a size of 60 mm in diameter and 30 mm in height for the BTS test (Fig. 5. ii)). For the UCS test, two loading plates with each having a size of 70 mm in diameter and 10 mm in height were placed at the top and bottom of the specimens and moved towards each other with a constant vertical loading rate of 5 cm/s to apply a uniaxial load on the cylindrical specimens through Coulomb frictional contacts. The cylindrical specimen was completely free except the contacts. The cylindrical model was discretised into 97,162 tetrahedral elements, 19,511 nodes and 143,639 initially zero-thickness cohesive elements. For the BTS test, two square loading plates with each having a length of 60 mm and a width of 30 mm were placed at the top and bottom of the specimens and moved towards each with a constant vertical loading rate of 5 cm/s, too. The BTS model was discretised into 64,513 tetrahedral elements, 12,307 nodes and 125,222 initially zero-thickness cohesive elements. The input parameters assigned to the models are obtained following an iterative calibration procedure until the stress-strain curve and the failure pattern from the simulations closely matched those obtained from the laboratory tests. Four sets of separate calibrations were performed for both control specimens and those subjected to 20, 40 and 60 freezing and thawing cycles. The input parameters obtained during the calibration procedures generate acceptable strength and elastic properties as well as fracture patterns, which, however, are not a unique set [45]. Although the loading velocity of the simulation is higher than that in the laboratory experiment, it has been demonstrated that a quasi-static loading condition is ensured through the artificial critical damping scheme with viscous damping coefficient [36], [46]. A mass scaling factor of 10 is further applied to reduce the computing time of the 3D FDEM simulations, which won't affect the obtained simulation results notably [36], [46].

It must be emphasized that the input parameters related to fracturing (i.e. tensile strength, cohesion, internal friction angle and fracture energies) in FDEM should be considered as microscale parameters and are different from the general macroscale mechanical parameters as obtained in the UCS and BTS tests. Meanwhile, the macroscopic input parameters including elastic modulus and Poisson's ratio, can be directly obtained from experimental tests. In quasi-static condition, gravity is neglected since the density has no physical meaning in this case. For model calibration purposes, it is convenient to classify the input parameters into the following categories: (1) penalty terms and numerical control parameters namely contact penalty, and cohesive penalty, (2) macroscopic parameters, including the elastic modulus (E), and Poisson's

ratio (ν), and (3) microscopic parameters including microscopic tensile strength, microscopic cohesion and microscopic internal friction angle. For (1), we follow the procedure for the determination of these values established in [36], [47]. For macroscopic physical parameters in (2) appropriate values can be directly established according to those from direct measurements. One of the most critical steps in modelling with FDEM is the calibration of input microscale parameters in (3). In general, the calibration process is a tedious trial and error process against the physical testing results. Table 1 lists the input parameters of the numerical modelling for the control specimen, which is defined as the specimen without subjecting to any freezing and thawing cycles and the specimens subjected to 60 freezing and thawing cycles which selected among three specimens with its UCS and elastic modulus closest to the average.

3. Experimental and numerical results and analyses

3.1. Deterioration of physical-mechanical properties of sandstones subjected to various freeze-thaw cycles

Table 2 summarizes the variations of the P-wave velocity, elastic modulus, UCS and BTS of the sandstones subjected to 0, 20, 40 and 60 freeze-thaw cycles. Fig. 6. i) illustrates the change of the P-wave velocity of the sandstone with the increasing number of freeze-thaw cycles. In terms of the average value, the P-wave velocity reduced by 9%, 23% and 24% after 20, 40 and 60 freeze-thaw cycles, respectively. The reason might be that the increased freeze-thaw cycles resulted in increased micro cracks, which led to the reduction of P-wave velocity. Moreover, the size of pores become larger with the freeze-thaw cycle increasing, which resulted in longer time for waves to transmit through the specimens due to longer path, or an increase in discontinuities leading the decrease of the P-wave velocity. As shown by the trend line in Fig. 6. i) there was a linear correlation between the P-wave velocity and the number of the freeze-thaw cycles.

As can be seen from Fig. 6. ii), the average value of BTS of sandstones decreases from 5.35 MPa to 5.24 MPa, 5.10 MPa and 5.06 MPa with the number of the freeze-thaw cycles increasing from 0 to 20, 40 and 60, respectively. In other words, the tensile strengths of the sandstones subjected to 20, 40 and 60 freeze-thaw cycles decrease by 2.1%, 4.4% and 5.5%, respectively. The sandstone specimens subjected to the increased number of freeze-thaw cycles have more microcracks [48], which decrease the ability of the sandstone for saving the strain energy and thus reduce BTS. The correlation between BTS and the number of freeze-thaw

cycles is also linear, as shown in Fig. 5, and the correlation coefficient is larger than that in the case of P-wave velocity.

The effect of the number of the freeze-thaw cycles on average value of UCS of the sandstone is depicted in Fig. 6. iii), which shows the average UCS of the sandstones changes from 37.84 MPa to 35.18 MPa, 32.98 MPa and 29.15 MPa as the number of the freeze-thaw cycles increases from 0 to 20, 40 and 60, respectively. Thus, the UCS of the sandstone decreases overall as the number of the freeze-thaw cycles increases. There are some deviations in some of results, which can be considered by the cause of inhomogeneity inside the specimens [49].

Since there are various microcracks induced by the freeze-thaw cycles in the sandstone specimens, these pre-existing microcracks with respect to the axial loading direction first close during the UCS test when the applied compressive stress reaches to the crack-closure stress. Further compressions induce local tensile stresses, which may exceed the local tensile strength at the tips of the pre-existing flaws and initiate the new cracks on those tips. Thereafter, these cracks propagate in a manner of wing cracks, parallel to the applied maximum principal stress [50] resulting in axial splitting. The increasing number of freeze-thaw cycles induces more freezing loads to be applied on the microcracks and pores in the sandstone. The freezing load then further increases the number and size of the microcracks and pores, which result in new microcracks generated by freeze-thaw cycles facilitating the crack propagation to occur during UCS discussed above. That is why, the UCS of sandstone reduces with the freeze-thaw cycles increasing. The correlation in Fig. 6. iii) is still approximately linear although the correlation coefficient is smaller.

Fig. 6. iv) shows the relationship between the elastic modulus of sandstones and the number of freeze-thaw cycles. It can be seen from Fig. 6. iv) that, when the number of freeze-thaw cycles is increased to 20, 40 and 50, the average elastic modulus reduces by 10.4%, 15.6%, and 16.9%, respectively, compared with that of the sandstone without subjecting to the freeze-thaw cycles. The correlation between the elastic modulus and the number of freeze-thaw cycles is also linear, as shown in Fig. 6. iv), and the correlation coefficient is larger than that in the case of P-wave velocity and UCS.

The mechanisms of the deterioration of the physical-mechanical properties of sandstones may be that the increased freeze-thaw cycles resulted in increased micro cracks. Jiang et al. [51] investigated the deterioration mechanisms using scanning electron microscope (SEM) and then concluded that the freeze-thaw cycles increased the width of microcracks resulting in

microscopic structure changes. Niu et al. [52] pointed out these microscopic structure changes of the rocks were due to the coupling effects of water and temperature variation after conducting experimental studies on crack coalescence behaviour of double unparallel fissure-contained sandstone specimens subjected to freeze-thaw cycles under uniaxial compression. The effect of water includes the dissolution and stress effects while temperature variation damages rocks by means of different temperature gradients and phase transitions of water during the freeze-thaw process [52], [53]. Moreover, Zhou et al. [54] and Niu et al. [52] investigated the microstructure around the crack tips in sandstones with and without subjecting to freeze-thaw cycles by SEM and concluded the nature of the failure of the flawed rock mass under freeze-thaw cycles lies in the fatigue damage of rocks. They further elaborated the stress fields around the tips of pre-existing fissures periodically redistributed due to the repeated frost-heaving actions in response to various freeze-thaw cycles, which led to the fatigue damage around these tips of the fissures and contributed to the failure evolution of the flawed rock mass. To better characterize the deterioration of the physical-mechanical properties of the Tasmanian sandstones subjected to the freeze-thaw cycles, a damage variable, *D*, is defined on the basis of the average uniaxial compressive strength as Eq. 1:

$$D = \frac{\bar{\sigma}_c - \bar{\sigma}_c'}{\bar{\sigma}_c} \quad \text{Eq. 1}$$

where $\bar{\sigma}_c$ is the average uniaxial compressive strength of the sandstone specimens without the freeze-thaw cycles and $\bar{\sigma}_c'$ is that of the specimens subjected to the freeze-thaw cycles. The damage variables obtained using Eq. 1 are summarized in Table 1 for the sandstones subjected to 0, 20, 40 and 60 freeze-thaw cycles, which clearly shows that the damage variable increases as the number of the freeze-thaw cycles increases.

3.2. Three-dimensional modelling of the failure process of the sandstones without subjecting to freeze-thaw cycles

Fig. 7. i) and ii) shows the modelled rock failure progressive process in terms of the distributions of the minor principal (i.e. compressive) stress and the damage variable [i.e., D, D=1 means macroscopic (broken) CE6 while D=0 corresponds to intact], respectively, at different loading stages (points A-F in the stress-strain curve in Fig. 7. iii) in the FDEM simulation of the UCS test for specimens without subjecting to freezing and thawing cycles. Fig. 7. i) A shows the stress in the specimen at the stage before the onset of nonlinearity in the stress-strain curve. The growth of unstable microscopic cracks commences as the loading

355 displacement continues and extends until the peak stress of the stress-strain curve is reached
356 (point B in Fig. 7. iii)). Afterwards, macroscopic cracks form due to the propagation and
357 coalescence of the microscopic cracks coalescence, which results in the loss of bearing capacity
358 of the sandstones. As can be seen in Fig. 7. i) C-E, the stress begins to decrease with increasing
359 strain (point C-E in Fig. 7. iii)). Finally, the formed macroscopic cracks propagate further,
360 resulting in the complete failure of sandstones (point F in Fig. 7. iii)).

361 Fig. 7. ii) shows the distributions of all damage (including pure mode-I, pure mode-II and
362 mixed-mode) (A-F-1) and pure mode-II damage (F-2) at different loading stages. As can be
363 seen from the comparison between Fig. 7. ii) A-F-1 and F-1, the tensile and mixed-mode
364 damage is the dominant failure mechanism at both pre-peak stage (A-B in Fig. 7. iii)) and post-
365 peak stage (C-F-1 in Fig. 7. iii)). The modelled tensile and mixed-mode failure mechanism is
366 consistent with the multiple axial splitting failures observed in the experiments considering the
367 limitation of FDEM in modelling pure mode I failure mechanism and usually treating it as
368 mixed-mode failure mechanism for the numerical simulations with unstructured meshes [29].
369 After that, at final stage of strain softening (F-1 in Fig. 7. iii)), the formed tensile and mixed-
370 mode cracks propagate and coalescence forming the axial splitting failure pattern.

371 Fig. 8. i) and ii) illustrates the modelled rock failure progressive process in terms of the
372 distributions of the horizontal stresses and the damage variable D at different loading stages
373 (points A-D in the stress-strain curve in Fig. 8. iii)) in the FDEM simulation of the BTS test. It
374 can be seen from Fig. 8. i) A that uniform tensile stress fields are formed around the central
375 line of the disc and there is no failure at the stage before the peak stress (points A in Fig. 8.
376 iii)). Once the indirect tensile strength of the rock is reached (points B in Fig. 8. iii)), tensile
377 macroscopic cracks initiate around the central diametrical line of the rock disc. After that, the
378 macroscopic cracks start to propagate along the central diametrical line, as shown in Fig. 8. i)
379 C. Till this stage, the tensile damage is the dominant failure mechanism, as indicated by the
380 mixed-mode damage in Fig. 8. ii) A-C. Finally, the further propagation and coalescence of the
381 formed macroscopic cracks split the rock disc into two halves (Fig. 8. ii) D), during which there
382 are some shear damages around the two loading locations. Thus, the modelled failure
383 mechanism and fracture pattern are consistent with those observed in the experiments.
384 However, the numerical modelling shows a single failure surface along the central diametrical
385 line of the disc while the experiment indicates multiple failure surfaces. Double checking of
386 the final fracture pattern in Fig. 8. ii) D reveals that there are multiple unmerged macro fractures
387 around the main fracture surface, which are similar to those observed in the BTS experiment.

3.3 Three-dimensional modelling of the failure process of the sandstones subject to various freeze-thaw cycles

Fig. 9. i) and ii) illustrates the modelled rock failure progressive process in terms of the distributions of the principal stress and the damage variable at different loading stages (points A-F in the stress-strain curve in Fig. 9. iii) in the FDEM simulation of the UCS test of the sandstone subjected to 60 freezing and thawing cycles. Fig. 9. i) A shows the stress distribution in the specimen at the pre-peak stress stage and the stress is lower than that at the same stage in the control model (Fig. 7. i) A). At the peak stress (point B in Fig. 9. iii)), which is smaller than that of the control model (Fig. 7. i) B), the microscopic cracks propagate form a macrocrack (Fig. 9. ii) B. As can be seen from Fig 9. i) C-E, the stress begins to decrease with increasing strain (point C-E in Fig. 9. iii)). At the final stage (Fig. 9. i) F), the formed macroscopic cracks propagate further, resulting in the complete failure of sandstones (point F in Fig. 9. iii)).

Fig. 9. ii) A-F-1 and F-2 show the distributions of all damage and the pure mode-II damage only, respectively, at different loading stages. It should be noted that all damage includes the pure mode-I, pure mode-II and mixed-mode damages. At the peak stress (point B in Fig. 9. iii)), the dominant failure mechanism is the tensile and mixed-mode damages, which is also more manifest than that in the previous modelling of the control specimen at the peak stress. Similar to the modelling of the control model, the macro cracks form after the peak stress and the mixed-mode damage continues to be the dominant failure mechanism (Fig. 9. ii) C-F-1). Finally, during the late strain-softening stage, the tensile and mixed-mode cracks propagate, interact and coalesce in the mode-II damage mechanism resulting in the final shear failure pattern (Fig. 9. ii) F-2).

The modelled failure progressive processes of the sandstone subjected to 60 freeze-thaw cycles in the BTS test are illustrated in Fig. 10. i), ii) and iii) in terms of the distributions of the horizontal stresses, the evolution of the damage variable D, and the completed stress-strain curve, respectively. Before the peak stress (point A in Fig. 10. iii), almost uniform tensile stresses around the central diametral line of the disc are observed again. At the peak load, the macroscopic cracks are initiated in the mixed-mode along the central diametrical line of the rock disc (Fig. 10. i) B). Compared with the control model, this model presents severe mixed-mode damages at this stage due to the low physical-mechanical parameters for the rock subjected to 60 freeze-thaw cycles. Afterward, the macroscopic cracks propagate along the

central diametrical line (Fig. 10. i) C) splitting the rock disc into two halves (Fig. 10. i) D). The comparison between the failure mechanisms shown in Fig. 10. ii) C (mixed-mode I-II damage only) and D (all damages) indicates that the mixed-mode damage is still dominant in the BTS modelling of the sandstone subjecting to various freezing and thawing cycles.

4 Discussions

4.1 Comparisons between the experimental and numerical stress-strain curves of the sandstones subject to various freeze-thaw cycles

Fig. 11. i-iv) compares the axial stress versus axial strain curves obtained from both experimental tests and numerical simulations of sandstones subjected to various freeze-thaw cycles in the UCS tests, in which, the crack initiation stress (dark blue colour marks) and peak stress (red colour marks) from both the laboratory tests and numerical simulations are marked and their values presented in Table 3. It can be seen from Fig. 11. that the experimental and numerical stress-strain curves agree well with each other in the terms of the linear elastic stage, crack initiation stress, nonlinear crack growth stage, peak strength, post-peak unstable crack growth stage and brittle failure behaviour although the numerical simulations fail to model the initial compaction stage. All stress-strain curves from the laboratory tests show a nonlinear downward concave shape in the initial compaction stage, which are omitted in Fig. 11. for the convenience of the comparisons between the laboratory tests and numerical simulations. The initial compaction stage is resultant from the closure of initial pores and fissures within the rocks subjected to various freeze-thaw cycles. The numerical simulations consider those initial pores and fissures caused by various freeze-thaw cycles through deteriorating the physical-mechanical parameters of the rocks. Thus, it is reasonable that the numerical simulation is unable to simulate the initial compaction stage. It is obvious from Fig. 11. and Table 3. that the linear elastic stage and crack initiation stress from the laboratory tests and numerical simulations are comparable, which also show that they decrease as the number of freeze-thaw cycles increases. The numerical simulations are able to capture the nonlinear crack growth stages, too, although the exact forms of the nonlinear crack growth stages are not the same as those from the laboratory tests. The peak strength and post-peak unstable crack growth stage of the stress-strain curves from the numerical simulation have an acceptable conformity with those from the experimental tests, too. However, the post-peak stress curves from the experimental tests become flatten with the number of freeze-thaw cycles increasing, i.e. somewhat ductile crack growth in the early phase of the post-peak unstable crack growth stage, which has not been captured by the numerical simulations. After that, a sudden loss of bearing

capacities does happen for all the stress-strain curves obtained from the laboratory tests, which is well captured by all numerical simulations.

4.2 Comparison between the experimental and numerical failure patterns of the sandstones subject to various freeze-thaw cycles

Fig. 12. compares the final failure patterns of of the sandstone specimens subjected to various freeze-thaw cycles in the UCS tests obtained from both laboratory experiments and numerical simulations. It is found that all specimens without undergoing freeze-thaw cycles failed in axial splitting during the laboratory UCS tests (Fig. 12. i)A). For the specimens subjected to 20 freeze-thaw cycles, one of the specimens still failed in axial splitting model while the other two specimens failed in shearing along a single plane during the laboratory UCS tests (Fig. 12. i) B). The failure mode of all the specimens subjecting to 40 freeze-thaw cycles changed to the shear failure although shearing along a single plane was only observed for one specimen and the other two specimens failed in double shear (Fig. 12. i) C). Moreover, all the specimens subjected to 60 freeze-thaw cycles failed in the shearing mode along a single plane (Fig. 12. i) D). Thus, the analysis of the failure mode shows that it changes from the axial splitting to various shear failure modes in the laboratory UCS tests of sandstones subjecting to with an increasing number of freeze-thaw cycles. Moreover, it is noted that the shearing along a single plane is the most common failure mode of the specimens in the laboratory UCS tests after subjecting to the freeze-thaw cycles. As it is clear from Fig. 12. ii) A, the failure pattern of the control specimen from the numerical simulations was axial splitting failure, which agrees with the experimental observation (Fig. 12. i) A). With the number of freeze-thaw cycles increasing, the failure pattern changed to the shear failure pattern, as shown in Fig. 12. ii) B, C and D which agrees with the experimental observation, too (Fig. 12. i) B, C and D).

Fig. 13. compares the final failure patterns of of the specimens subjected to various freeze-thaw cycles in the BTS tests obtained from both laboratory experiments and numerical simulations. It can be seen from Fig. 13. A that the failure pattern of the specimens subjecting to zero freeze-thaw cycles from both laboratory experiments and numerical simulations was central multiple splitting fractures. The failure pattern of central multiple splitting fractures is the dominant failure mode in the BTS test of sandstones with a relatively higher tensile strength since the central multiple splitting fractures are developed in order to release the stored high strain energy. The main failure pattern changed to a central fracture for most of the specimens

484 treated by various freeze-thaw cycles Fig. 13. B-D, which can be explained by the increasing
485 number of microcracks in sandstones caused by various numbers of freeze-thaw cycles.

486 The change of the failure patterns from the axial splitting failure to shear failure in the UCS
487 tests and those from the central multiple splitting failures to the central single fracture in the
488 BTS tests can be explained in terms of the pre-existing cracks, the local fatigue-damage zones
489 around these pre-existing cracks caused by the freezing and thawing cycles [51, 53], and their
490 propagations during the uniaxial loading of the sandstones subjected to various freeze-thaw
491 cycles. Under uniaxial loading in the UCS test, the pre-existing cracks become free to
492 propagate when they are aligned parallel to the maximum principal stress (mostly tensile). In
493 other words, the specimen fails in axial splitting mode when the microstructure of a specimen
494 cannot prevent the propagation of these cracks [55], which is the case for the sandstone without
495 subjecting to the freeze-thaw cycles. For the sandstone subjected to the freeze-thaw cycles,
496 local fatigue-damaged zones form around the pre-existing cracks according to [51, 53], which
497 are further motivated during the loading process. When the compressive loads are applied
498 during the UCS tests, the pre-existing cracks propagate through these local fatigue damaged
499 zones. Since these local fatigue damaged zones are not necessary to be parallel to the maximum
500 principal stress, the coalescences of the pre-existing cracks take place in adjacent or in close
501 proximity to the tips of the suitably oriented microcracks and releases the strain energy in the
502 form of shear failure, which is why macroscopic shear failure patterns are observed during the
503 UCS tests of the sandstones subjected to more freeze-thaw cycles. Similarly, during the BTS
504 tests of the sandstones without subject to the freeze-thaw cycles, the pre-existing cracks aligned
505 along the loading diametral line are forced to initiate and propagate resulting in smooth central
506 splitting fracture patterns. For the sandstone samples subjected to various freeze-thaw cycles,
507 the freeze-thaw cycles induce the local fatigue-damaged zones around the tips of the pre-
508 existing cracks, which cause the pre-existing crack to initiate, propagate and coalesce through
509 these local fatigue-damage zones resulting in more zigzag central splitting fracture patterns.

510 However, the 3D numerical simulations model the random pre-existing defects in sandstones
511 through non-uniform meshes and model the freeze-thaw induced damages through
512 deteriorating physical-mechanical properties of the sandstones subjected to various freeze-
513 thaw cycles. Thus, the 3D numerical simulations fail to capture the local fatigue-damaged
514 zones around the tips of the pre-existing defects due to the freeze-thaw cycles although the 3D
515 numerical simulations well capture the deterioration mechanism and failure process of the

sandstones including the transition of the failure patterns of the sandstones with the number of freeze-thaw cycles increasing.

5. Conclusions

A series of laboratory tests were firstly conducted to investigate the physical-mechanical behaviours of Tasmanian sandstones subjected to different freezing and thawing cycles, which includes P-wave velocity, UCS, BTS and freeze-thaw tests. A self-developed 3D GPGPU-parallelized FDEM is then employed to model the failure processes of these sandstones with the focus on clarifying the damage mechanisms of the sandstones subjected to various freeze-thaw cycles. The following specific conclusions were obtained:

- The laboratory tests showed that P-wave velocity, UCS and BTS of Tasmanian sandstones reduced with the number of freeze-thaw cycles increasing. Their reduction rates from 0 to 20 freeze-thaw cycles were higher than those from 20 to 40 cycles and from 40 to 60 cycles.
- The main failure pattern of the sandstone changed from axial splitting to shearing in the UCS tests and from smooth central fractures to a zigzag central fracture in the BTS tests with the number of freeze-thaw cycles increasing.
- The GPGPU-parallelized 3D modelling reproduces the failure processes of Tasmanian sandstones subjected to various freeze-thaw cycles in the UCS and BTS tests, which validates the experimental observations that the physical-mechanical parameters of the sandstone degrade with the increasing number of freeze-thaw cycles.
- The 3D modelling clarifies the deterioration and failure mechanisms of sandstones subjected to various freeze-thaw cycles. For the sandstone without subjecting to freeze-thaw cycles, axial splitting is the main failure pattern in the UCS test since tensile and mixed-mode damages are dominant failure mechanisms observed in the corresponding 3D modelling. For the sandstones subjecting to various freeze-thaw cycles, the increasing number of freeze-thaw cycles causes the macroscopic cracks initiated and nucleated by the tensile and mixed-mode damages to propagate, interact and coalesce in the mode-II failure mechanisms resulting in the final shear fracture pattern in the UCS test. For both the control model and that subjected to freezing and thawing cycles in the BTS test, a central splitting fracture is the dominant failure pattern, which, however, is accompanied by zigzag fractures in the BTS test of the specimens subject to various freeze-thaw cycles.

Acknowledgements

The first author would like to thank the support of Tasmanian Postgraduate Research Scholarships which enable him to conduct his PhD study at University of Tasmania.

Data availability

The raw/processed data required to reproduce these findings are available from the corresponding author upon request.

References

[1] D. A. Streletskiy, N. I. Shiklomanov, and F. E. Nelson, "Permafrost, Infrastructure, and Climate Change: A GIS-Based Landscape Approach to Geotechnical Modeling," *Arctic, Antarct. Alp. Res.*, vol. 44, no. 3, pp. 368–380, 2012.

[2] "Australian Antarctic Division." [Online]. Available: http://www.antarctica.gov.au.

[3] Y. Zhang and R. L. Michalowski, "Thermal-Hydro-Mechanical Analysis of Frost Heave and Thaw Settlement," *J. Geotech. Geoenvironmental Eng.*, vol. 141, no. 7, p. 04015027, 2015.

[4] G. Sinnathamby, H. Gustavsson, and L. Korkiala-tanttu, "Frost Heave and Thaw Settlement Estimation of a Frozen Ground Frost Heave and Thaw Settlement Estimation of a Frozen Ground," no. November, 2015.

[5] G. Krinner *et al.*, "Long-term climate change: Projections, commitments and irreversibility," *Clim. Chang. 2013 Phys. Sci. Basis Work. Gr. I Contrib. to Fifth Assess. Rep. Intergov. Panel Clim. Chang.*, vol. 9781107057, pp. 1029–1136, 2013.

[6] Y. Zhang, "Thermal-Hydro-Mechanical Model for Freezing and Thawing of Soils," 2014.

[7] G. F. Gambino and J. P. Harrison, "Rock Engineering Design in Frozen and Thawing Rock: Current Approaches and Future Directions," *Procedia Eng.*, vol. 191, no. June, pp. 656–665, 2017.

[8] N. Matsuoka and J. Murton, "Frost weathering: recent advances and future directions," *Permafr. Periglac. Process.*, vol. 19, no. 2, pp. 195–210.

[9] M. Krautblatter, D. Funk, and F. K. Günzel, "Why permafrost rocks become unstable: A rock-ice-mechanical model in time and space," *Earth Surf. Process. Landforms*, vol. 38, no. 8, pp. 876–887, 2013.

[10] X. Tan, W. Chen, J. Yang, and J. Cao, "Laboratory investigations on the mechanical properties degradation of granite under freeze–thaw cycles," *Cold Reg. Sci. Technol.*, vol. 68, no. 3, pp. 130–138, Sep. 2011.

[11] F. Bayram, "Predicting mechanical strength loss of natural stones after freeze–thaw in cold regions," *Cold Reg. Sci. Technol.*, vol. 83–84, pp. 98–102, Dec. 2012.

[12] İ. İnce and M. Fener, "A prediction model for uniaxial compressive strength of deteriorated pyroclastic rocks due to freeze–thaw cycle," *J. African Earth Sci.*, vol. 120, pp. 134–140, Aug. 2016.

[13] P. Wang, J. Xu, S. Liu, S. Liu, and H. Wang, "A prediction model for the dynamic mechanical degradation of sedimentary rock after a long-term freeze-thaw weathering: Considering the strain-rate effect," *Cold Reg. Sci. Technol.*, vol. 131, pp. 16–23, Nov. 2016.

[14] J. C. Jaeger, “Shear Failure of Anistropic Rocks,” *Geol. Mag.*, vol. 97, no. 01, p. 65, Feb. 1960.

[15] Y. M. Tien and M. C. Kuo, “A failure criterion for transversely isotropic rocks,” *Int. J. Rock Mech. Min. Sci.*, vol. 38, no. 3, pp. 399–412, Apr. 2001.

[16] Y. M. Tien, M. C. Kuo, and C. H. Juang, “An experimental investigation of the failure mechanism of simulated transversely isotropic rocks,” *Int. J. Rock Mech. Min. Sci.*, vol. 43, no. 8, pp. 1163–1181, Dec. 2006.

[17] Y.-K. Lee and S. Pietruszczak, “Application of critical plane approach to the prediction of strength anisotropy in transversely isotropic rock masses,” *Int. J. Rock Mech. Min. Sci.*, vol. 45, no. 4, pp. 513–523, Jun. 2008.

[18] O. Saeidi, V. Rasouli, R. G. Vaneghi, R. Gholami, and S. R. Torabi, “A modified failure criterion for transversely isotropic rocks,” *Geosci. Front.*, vol. 5, no. 2, pp. 215–225, Mar. 2014.

[19] M. Asadi and M. H. Bagheripour, “Modified criteria for sliding and non-sliding failure of anisotropic jointed rocks,” *Int. J. Rock Mech. Min. Sci.*, vol. 73, pp. 95–101, Jan. 2015.

[20] M. Singh, N. K. Samadhiya, A. Kumar, V. Kumar, and B. Singh, “A nonlinear criterion for triaxial strength of inherently anisotropic rocks,” *Rock Mech. Rock Eng.*, vol. 48, no. 4, pp. 1387–1405, Jul. 2015.

[21] X. Tan, H. Konietzky, T. Frühwirt, and D. Q. Dan, “Brazilian Tests on Transversely Isotropic Rocks: Laboratory Testing and Numerical Simulations,” *Rock Mech. Rock Eng.*, vol. 48, no. 4, pp. 1341–1351, Jul. 2015.

[22] J. Yu, X. Chen, H. Li, J. Zhou, and Y. Cai, “Effect of freeze-thaw cycles on mechanical properties and permeability of red sandstone under triaxial compression,” *J. Mt. Sci.*, vol. 12, no. 1, pp. 218–231, Jan. 2015.

[23] P. Wang, J. Xu, X. Fang, P. Wang, G. Zheng, and M. Wen, “Ultrasonic time-frequency method to evaluate the deterioration properties of rock suffered from freeze-thaw weathering,” *Cold Reg. Sci. Technol.*, vol. 143, no. June 2016, pp. 13–22, 2017.

[24] N. Matsuoka, “Microgelivation versus macrogelivation: Towards bridging the gap between laboratory and field frost weathering,” *Permafr. Periglac. Process.*, vol. 12, no. 3, pp. 299–313, 2001.

[25] K. M. Neaupane, T. Yamabe, and R. Yoshinaka, “Simulation of a fully coupled thermo–hydro–mechanical system in freezing and thawing rock,” *Int. J. Rock Mech. Min. Sci.*, vol. 36, no. 5, pp. 563–580, 1999.

[26] Y. W. Bekele, H. Kyokawa, A. M. Kvarving, T. Kvamsdal, and S. Nordal, “Isogeometric analysis of THM coupled processes in ground freezing,” *Comput. Geotech.*, vol. 88, pp. 129–145, 2017.

[27] X. Luo, N. Jiang, X. Fan, N. Mei, and H. Luo, “Effects of freeze-thaw on the determination and application of parameters of slope rock mass in cold regions,” *Cold Reg. Sci. Technol.*, vol. 110, pp. 32–37, 2015.

[28] H. Lin, D. Lei, R. Yong, C. Jiang, and S. Du, “Analytical and numerical analysis for frost heaving stress distribution within rock joints under freezing and thawing cycles,” *Environ. Earth Sci.*, vol. 79, no. 12, pp. 1–17, 2020.

[29] Y. I. Fogue-Djombou, S. Corn, L. Clerc, D. Salze, and E. Garcia-Diaz, “Freeze-thaw resistance of limestone roofing tiles assessed through impulse vibration monitoring and finite element modeling in relation to their microstructure,” *Constr. Build. Mater.*, vol. 205, pp. 656–

667, 2019.

[30] J. Bi, X. P. Zhou, and Q. H. Qian, “The 3D Numerical Simulation for the Propagation Process of Multiple Pre-existing Flaws in Rock-Like Materials Subjected to Biaxial Compressive Loads,” *Rock Mech. Rock Eng.*, vol. 49, no. 5, pp. 1611–1627, 2016.

[31] X. P. Zhou and J. Bi, “3D Numerical Study on the Growth and Coalescence of Pre-existing Flaws in Rocklike Materials Subjected to Uniaxial Compression,” *Int. J. Geomech.*, vol. 16, no. 4, 4015096, 2016.

[32] Y. Wang, X. Zhou, Y. Wang, and Y. Shou, “A 3-D conjugated bond-pair-based peridynamic formulation for initiation and propagation of cracks in brittle solids,” *Int. J. Solids Struct.*, vol. 134, pp. 89–115, 2018.

[33] Y. T. Wang, X. P. Zhou, and M. M. Kou, “Three-dimensional numerical study on the failure characteristics of intermittent fissures under compressive-shear loads,” *Acta Geotech.*, vol. 14, no. 4, pp. 1161–1193, 2019.

[34] M. Mohammadnejad, S. Dehkhoda, D. Fukuda, H. Liu, and A. Chan, “GPGPU-parallelised hybrid finite-discrete element modelling of rock chipping and fragmentation process in mechanical cutting,” *J. Rock Mech. Geotech. Eng.*, vol. 12, no. 2, pp. 310–325, Apr. 2020.

[35] D. Fukuda, M. Mohammadnejad, H. Liu, S. Dehkhoda, and A. Chan, “Development of a GPGPU-parallelized hybrid finite-discrete element method for modeling rock fracture,” *Int. J. Numer. Anal. Methods Geomech.*, vol. 43, no. 10, pp. 1797–1824, Jul. 2019.

[36] D. Fukuda, M. Mohammadnejad, H. Liu, Q. Zhang, and J. Zhao, “Development of a 3D Hybrid Finite-Discrete Element Simulator Based on GPGPU-Parallelized Computation for Modelling Rock Fracturing Under Quasi-Static and Dynamic Loading Conditions,” *Rock Mech. Rock Eng.*, vol. 53, no. 3, pp. 1079–1112, Mar. 2020.

[37] *The ISRM Suggested Methods for Rock Characterization, Testing and Monitoring: 2007-2014*. Springer International Publishing, 2015.

[38] P. Wang, J. Xu, X. Fang, and P. Wang, “Energy dissipation and damage evolution analyses for the dynamic compression failure process of red-sandstone after freeze-thaw cycles,” *Eng. Geol.*, vol. 221, pp. 104–113, 2017.

[39] M. Mutlutürk, R. Altindag, and G. Türk, “A decay function model for the integrity loss of rock when subjected to recurrent cycles of freezing-thawing and heating-cooling,” *Int. J. Rock Mech. Min. Sci.*, vol. 41, no. 2, pp. 237–244, Feb. 2004.

[40] Q. Ma, D. Ma, and Z. Yao, “Influence of freeze-thaw cycles on dynamic compressive strength and energy distribution of soft rock specimen,” *Cold Reg. Sci. Technol.*, vol. 153, no. March 2017, pp. 10–17, 2018.

[41] H. Y. Liu, Y. M. Kang, and P. Lin, “Hybrid finite–discrete element modeling of geomaterials fracture and fragment muck-piling,” *Int. J. Geotech. Eng.*, vol. 9, no. 2, pp. 115–131, 2015.

[42] A. A. Munjiza, *The Combined Finite-Discrete Element Method*. Wiley, 2004.

[43] H. Y. Liu, H. Han, H. M. An, and J. J. Shi, “Hybrid finite-discrete element modelling of asperity degradation and gouge grinding during direct shearing of rough rock joints,” *Int. J. Coal Sci. Technol.*, vol. 3, no. 3, pp. 295–310, 2016.

[44] A. Munjiza and K. R. F. Andrews, “Penalty function method for combined ÿnite–discrete element systems comprising large number of separate bodies,” *Int. J. Numer. METHODS Eng. Int. J. Numer. Meth. Engng*, vol. 49, no. January 1999, pp. 1377–1396, 2000.

[45] B. S. A. Tatone and G. Grasselli, “A calibration procedure for two-dimensional laboratory-scale hybrid finite–discrete element simulations,” *Int. J. Rock Mech. Min. Sci.*, vol. 75, pp. 56–

679 72, Apr. 2015.

680 [46] T. Heinze, G. Jansen, B. Galvan, and S. A. Miller, "Systematic study of the effects of mass and
681 time scaling techniques applied in numerical rock mechanics simulations," *Tectonophysics*,
682 vol. 684, pp. 4–11, 2016.

683 [47] M. Mohammadnejad, D. Fukuda, H. Y. Liu, S. Dehkhoda, and A. Chan, "GPGPU-parallelized
684 3D combined finite–discrete element modelling of rock fracture with adaptive contact
685 activation approach," *Comput. Part. Mech.*, vol. 7, no. 5, pp. 849–867, 2020.

686 [48] B. Ke, J. Zhang, H. Deng, and X. Yang, "Dynamic characteristics of sandstone under coupled
687 static-dynamic loads after freeze-thaw cycles," *Appl. Sci.*, vol. 10, no. 10, 2020.

688 [49] K. Park, K. Kim, K. Lee, and D. Kim, "Analysis of effects of rock physical properties changes
689 from freeze-thaw weathering in Ny-Ålesund region: Part 1-experimental study," *Appl. Sci.*,
690 vol. 10, no. 5, 2020.

691 [50] A. Bobet and H. H. Einstein, "Fracture coalescence in rock-type materials under uniaxial and
692 biaxial compression," *Int. J. Rock Mech. Min. Sci.*, vol. 35, no. 7, pp. 863–888, Oct. 1998.

693 [51] H. Jiang, Z. Mo, X. Hou, and H. Wang, "Association rules between the microstructure and
694 physical mechanical properties of rock-mass under coupled effect of freeze-Thaw cycles and
695 large temperature difference," *Sains Malaysiana*, vol. 46, no. 11, pp. 2215–2221, 2017.

696 [52] Y. Niu, X. P. Zhou, J. Z. Zhang, and Q. H. Qian, "Experimental study on crack coalescence
697 behavior of double unparallel fissure-contained sandstone specimens subjected to freeze-thaw
698 cycles under uniaxial compression," *Cold Reg. Sci. Technol.*, vol. 158, pp. 166–181, 2019.

699 [53] Q. Wang, J. Liu, X. Zhu, J. Liu, and Z. Liu, "The experiment study of frost heave
700 characteristics and gray correlation analysis of graded crushed rock," *Cold Reg. Sci. Technol.*,
701 vol. 126, no. August 2007, pp. 44–50, 2016.

702 [54] X. P. Zhou, Y. Niu, J. Z. Zhang, X. C. Shen, Y. Zheng, and F. Berto, "Experimental study on
703 effects of freeze-thaw fatigue damage on the cracking behaviors of sandstone containing two
704 unparallel fissures," *Fatigue Fract. Eng. Mater. Struct.*, vol. 42, no. 6, pp. 1322–1340, 2019.

705 [55] A. Basu, D. A. Mishra, and K. Roychowdhury, "Rock failure modes under uniaxial
706 compression, Brazilian, and point load tests," *Bull. Eng. Geol. Environ.*, vol. 72, no. 3–4, pp.
707 457–475, 2013.

708

709 List of Tables

715

716

717 List of Figures

768 Table 1. Physical-mechanical properties of Tasmanian sandstones subject to various freeze-thaw (F-
769 T) cycles

Specimen	Number of F-T Cycles	P-wave before F-T (m/s)	P-wave after F-T (m/s)	BTS (MPa)	UCS (MPa)	Elastic Modulus (GPa)	Average damage variable
S0-1	0	2448	-	5.53	30.93	4.5	
S0-2		2843	-	5.87	38.93	7.9	0
S0-3		2815	-	5.17	36.76	7.7	
S20-1	20	2192	1697	5.97	27.70	5.6	
S20-2		2816	2646	4.82	39.59	8.2	0.07
S20-3		2758	2539	4.91	38.26	7.1	
S40-1	40	2659	2297	4.67	34.06	6.7	
S40-2		2821	2443	5.57	42.16	9.9	0.13
S40-3		2820	2492	5.11	31.89	6.3	
S60-1	60	2753	1262	5.10	22.90	4.9	
S60-2		2845	2389	5.23	30.40	6	0.23
S60-3		2618	2323	4.83	34.16	7.3	

770
771
772
773
774
775
776
777
778
779
780
781
782
783
784
785
786
787
788
789
790
791
792

793 Table 2. Input parameters used in the FDEM simulations of the behaviour of the control specimens and
794 the specimens subjected to 60 freezing and thawing cycles in the UCS tests

Parameter	Unit	Control	60 freeze-thaw cycles
Density	kg/m^3	2200	2200
Young's modulus	GPa	7.7	6.1
Poisson's ratio	-	0.25	0.25
Microscopic tensile strength	MPa	5.35	5.05
Microscopic cohesion	MPa	10	7.7
Microscopic internal friction angle	^{o}	25.5	25.5
Microscopic mode I fracture energy	J/m^2	80	50
Microscopic mode II fracture energy	J/m^2	300	180
Normal contact penalty	GPa	77	61
Cohesive normal penalty	GPa	770	610
Cohesive tangential penalty	GPa	770	610

795
796
797
798
799
800
801
802
803
804
805
806
807
808
809
810
811
812
813
814
815
816
817

818 Table 3. Comparisons between the experimental and numerical stress and elastic modulus

		Crack initiation stress (MPa)	Peak strength (MPa)	Elastic modulus (GPa)
Control	Experimental	36.88	38.93	7.9
	Numerical	37.07	38.50	7.5
20 Freeze-Thaw cycles	Experimental	34.72	38.26	7.1
	Numerical	32.37	34.30	6.7
40 Freeze-Thaw cycles	Experimental	29.69	31.89	6.3
	Numerical	28.70	31.69	6.2
60 Freeze-Thaw cycles	Experimental	28.03	30.40	6.0
	Numerical	27.42	29.38	6.1

819
820
821
822
823
824
825
826
827
828
829
830
831
832
833
834
835
836
837
838
839
840
841
842
843
844

Fig. 1. Pundit PL-200 equipment for measuring P-wave velocities of the cylindrical rock specimens

i) Climatic controlled cabinet together with a assembly of tested samples

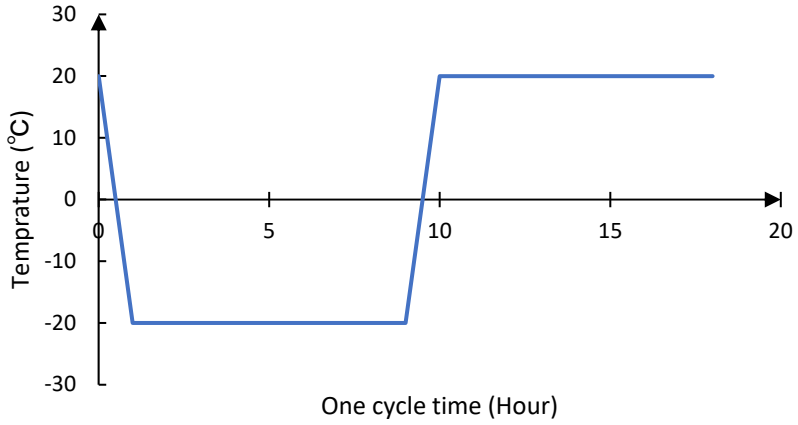

ii). Generalized temperature versus time curve of one freeze-thaw cycle

868 Fig. 2. Climatic controlled cabinet for the freeze-thaw tests

869

870

871

872

873

874

875

876

877

878

879

880

881 Fig. 3. Servo-controlled high stability compression testing apparatus for the UCS and BTS tests

882

883

884

885

886

887

888

889

890

891

892

893

894

895

896

897

898

899

900

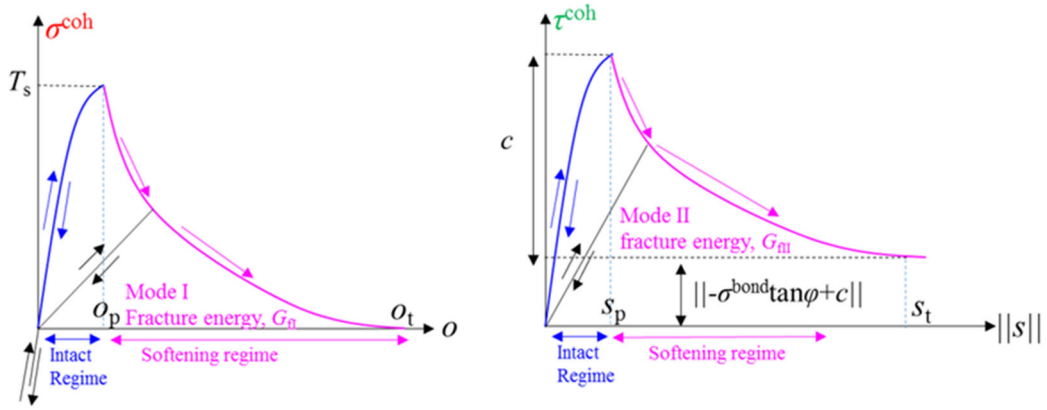

i) Under tension conditions

ii) Under shear and sliding conditions

Fig. 4. Constitutive behaviour of cohesive elements under the tension and shear & sliding conditions: i) under tension conditions, and ii) under shear and sliding conditions (Modified after [36])

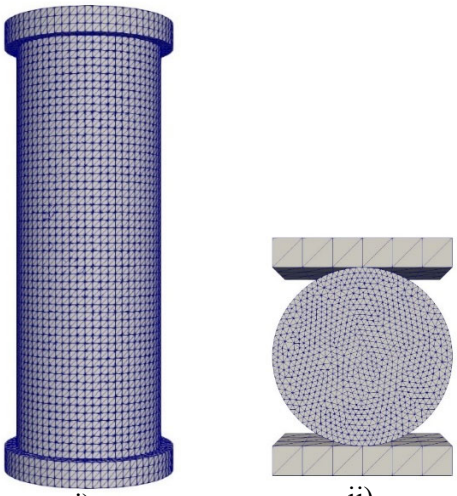

Fig. 5. 3D numerical models for simulating the behaviour of the sandstones in the UCS and BTS tests: i) UCS and ii) BTS

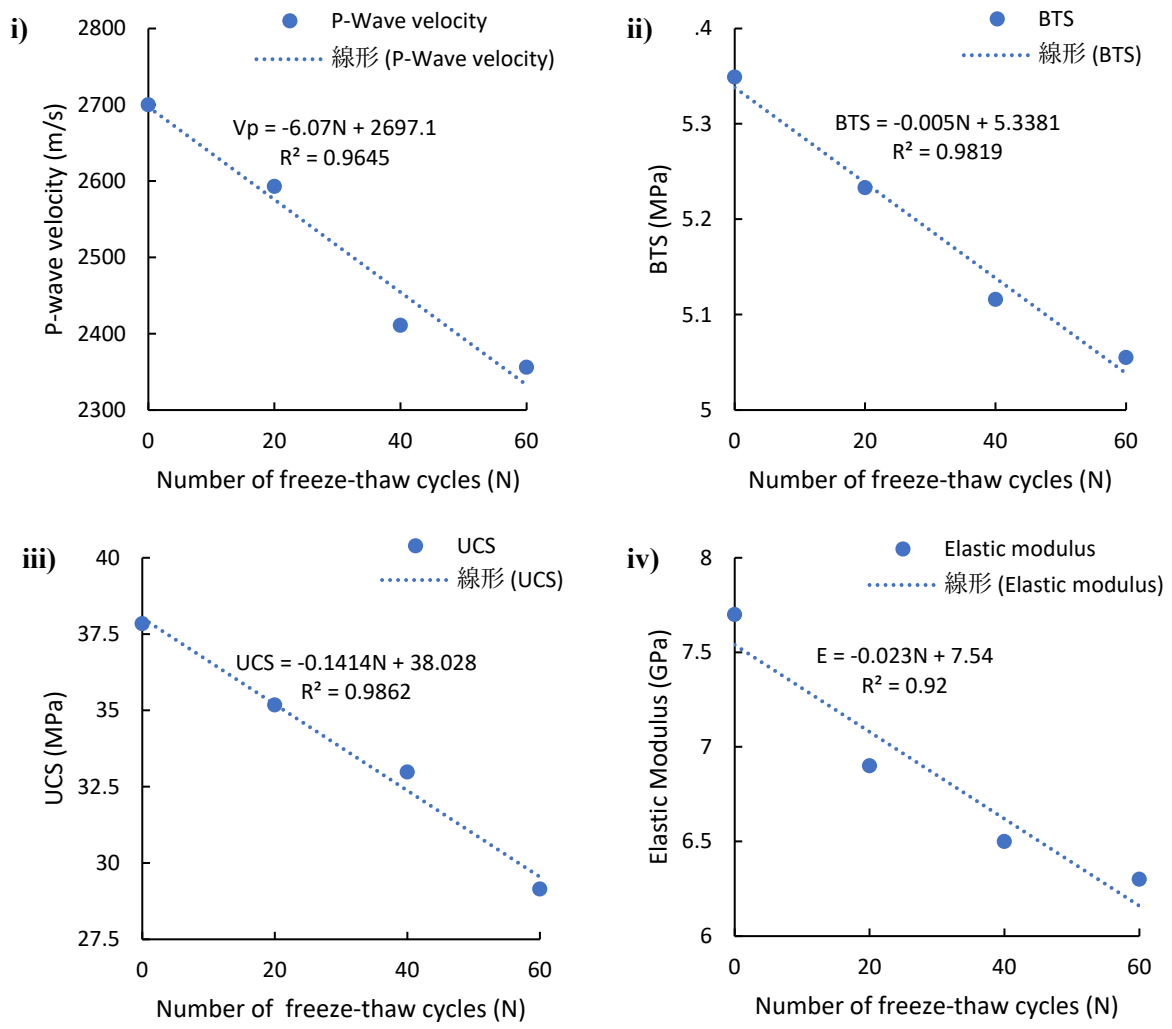

Fig. 6. Deterioration of the physical-mechanical parameters of the sandstones subjected to various freeze-thaw cycles i) P-Wave velocity, ii) Brazilian tensile strength, iii) uniaxial compressive strength, and iv) elastic modulus

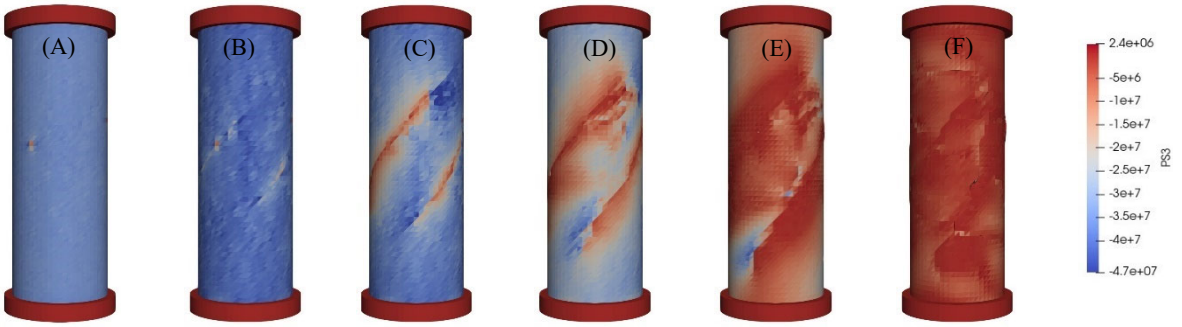

i) Distribution of minor principal (compressive) stresses

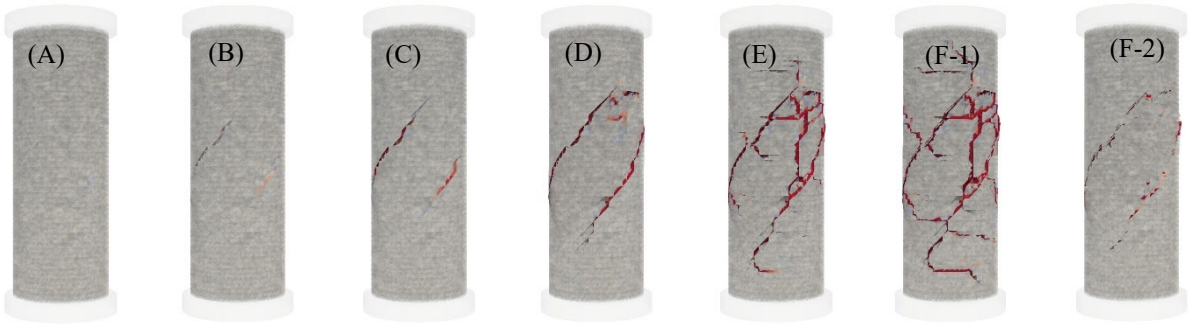

ii) Distribution of the damage variable (A-E and F-1: all damage including pure mode-I, pure mode-II and mixed-mode while F-2: pure mode-II damage only)

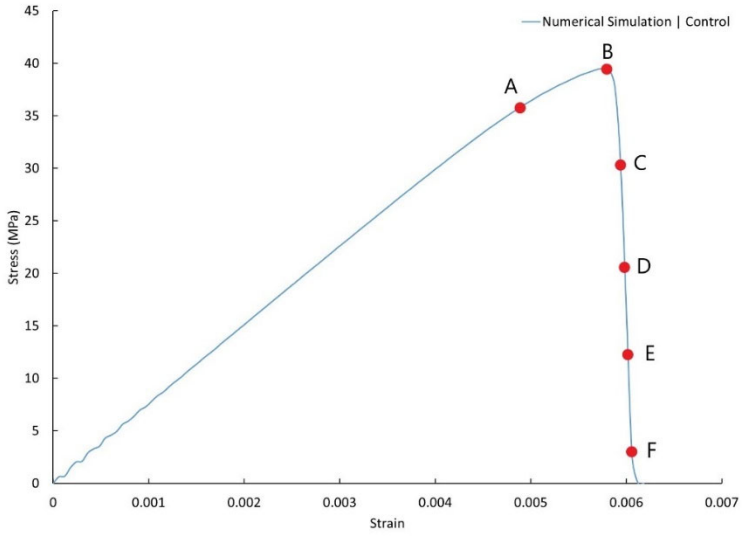

iii) Stress-strain curve

962 Fig. 7. 3D modelling of the failure process of the sandstones without subjecting to any freeze-thaw
963 cycles in the UCS test: i) Distribution of minor principal (most compressive) stresses in selected loading
964 steps, ii) Distribution of the damage variable in selected loading steps, and iii) Stress-strain curve

965

966

967

968

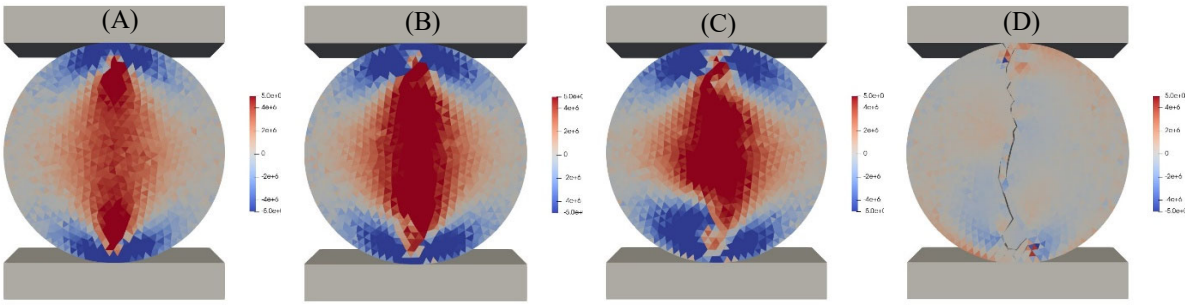

i) Distribution of horizontal stresses

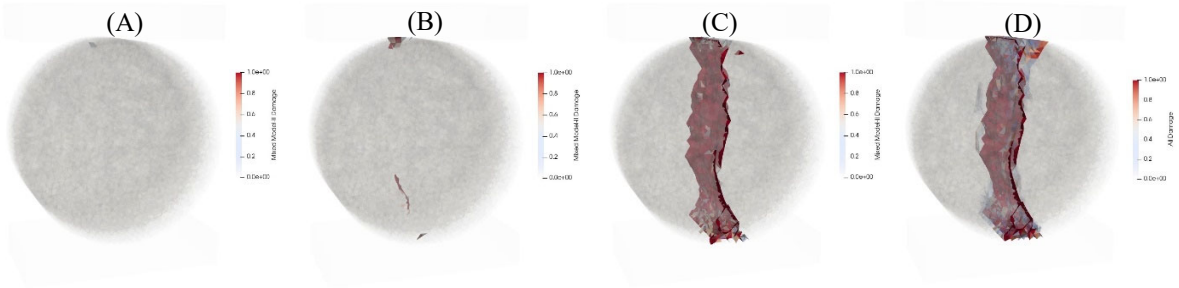

ii) Distribution of the damage variable

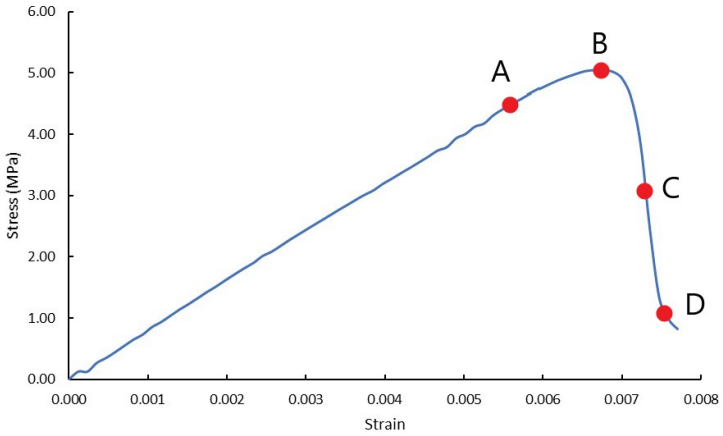

iii) Stress-strain curve

969 Fig. 8. 3D modelling of the failure process of the sandstones without subjecting to any freeze-thaw
970 cycles in the BTS test: i) Distribution of horizontal stresses, ii) Distribution of the damage variable,
971 and iii) Stress-strain curve

972

973

974

975

976

977

978

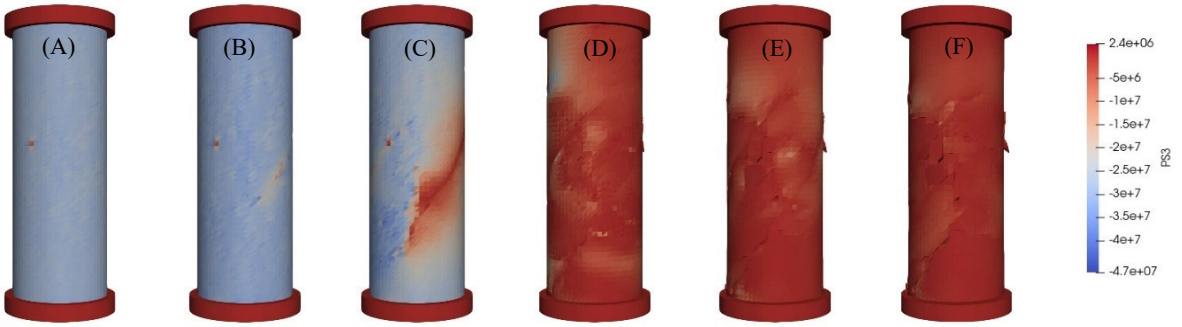

i) Distribution of minor principal (compressive) stresses

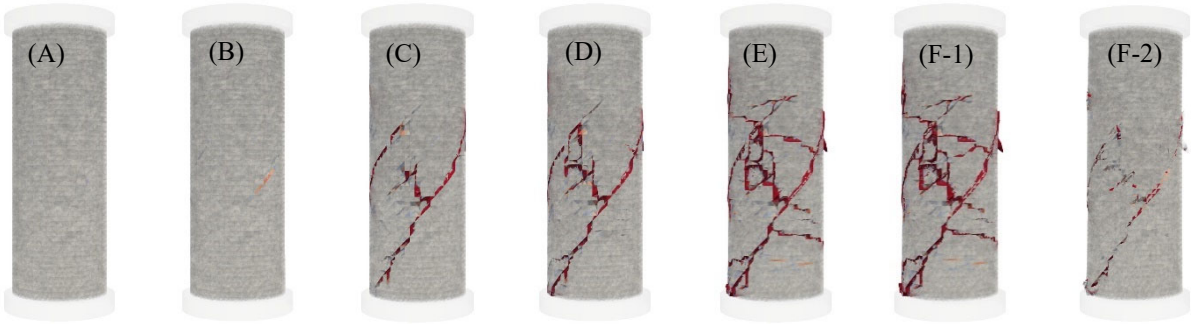

ii) Distribution of the damage variable (A-E and F-1: all damage including pure mode-I, pure mode-II and mixed-mode while F-2: pure mode-II damage only)

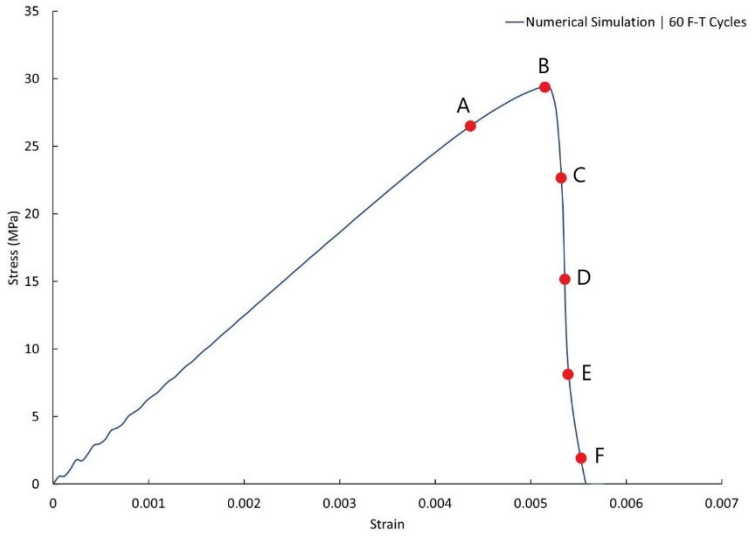

iii) Stress-strain curve

Fig. 9. 3D modelling of the UCS test of the sandstone subjected to 60 freeze-thaw cycles: i) Distribution of minor principal (most compressive) stresses in selected loading steps, ii) Distribution of the damage variable in selected loading steps, and iii) Stress-strain curve

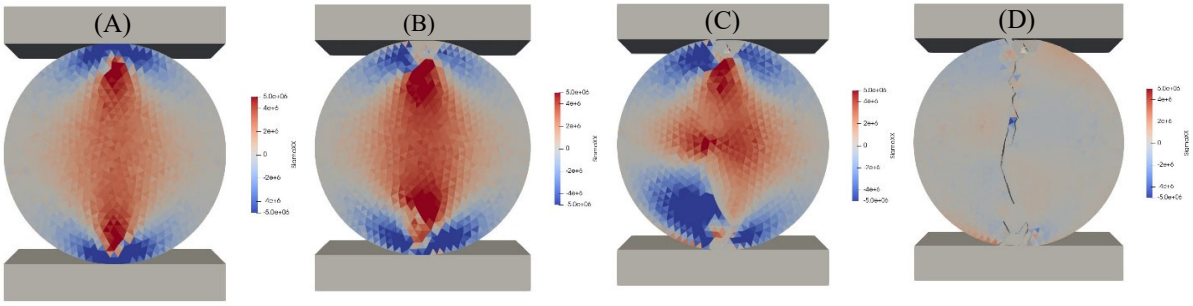

i) Distribution of horizontal stresses

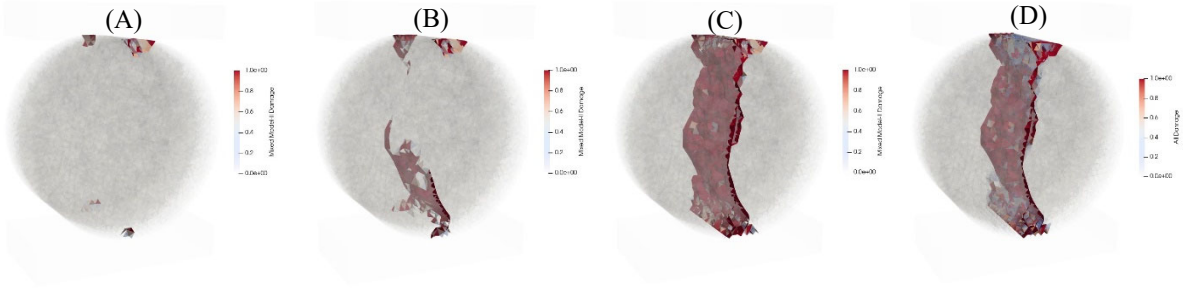

ii) Distribution of the damage variable

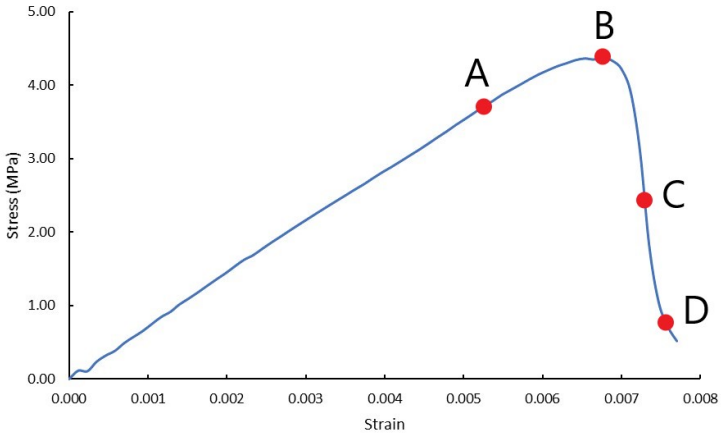

iii) Stress-strain curve

Fig. 10. 3D model of the BTS test for the sandstone subjected to 60 freezing and thawing cycles: i) Distribution of horizontal stresses, ii) Distribution of the damage variable, and iii) Stress-strain curve

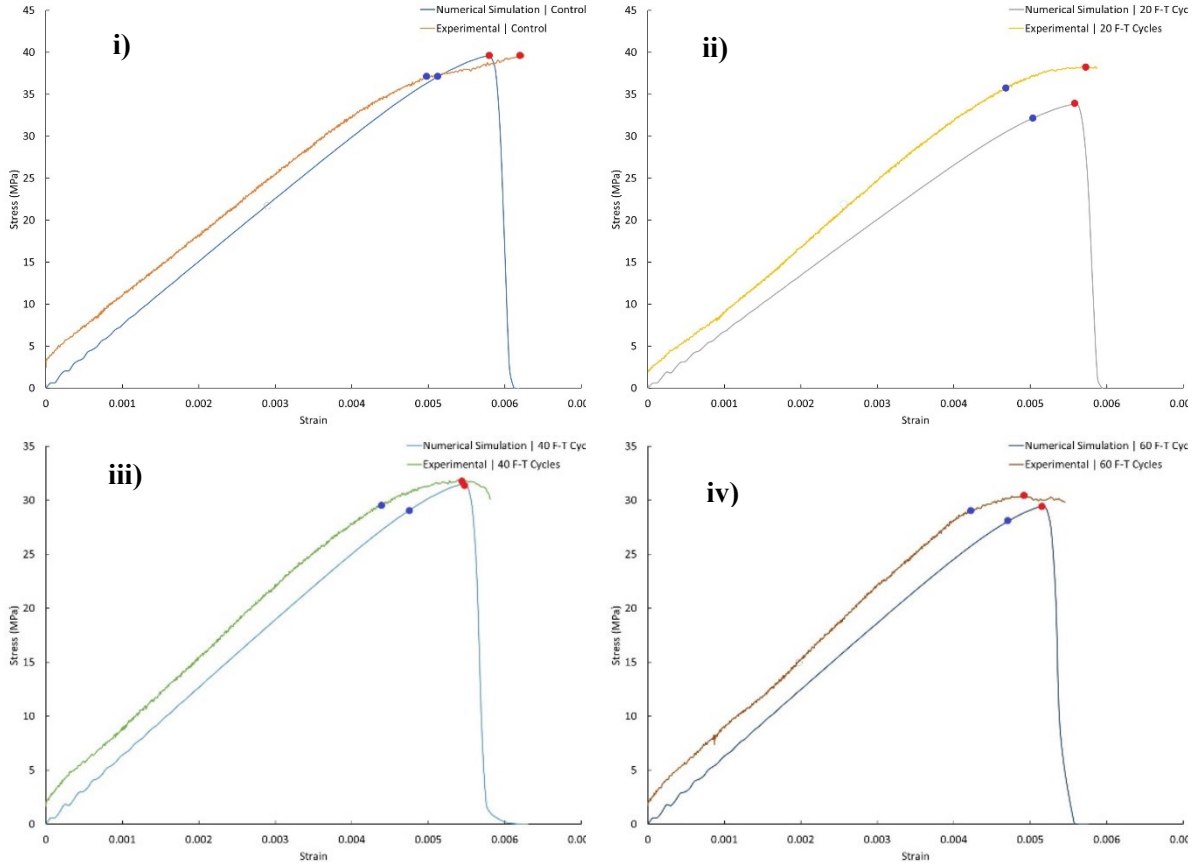

Fig. 11. Comparisons of the stress-Strain curves from both experimental tests and numerical simulations of the UCS tests of the sandstones subjected to various freezing and thawing cycles: i) 0 freeze-thaw cycle, ii) 20 freeze-thaw cycles, iii) 40 freeze-thaw cycles, and iv) 60 freeze-thaw cycles

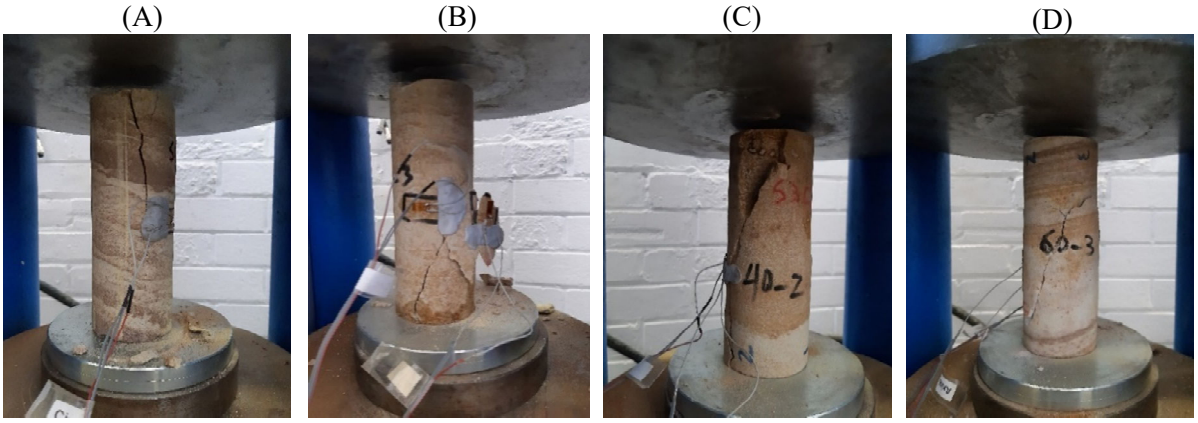

i) Laboratory experiments

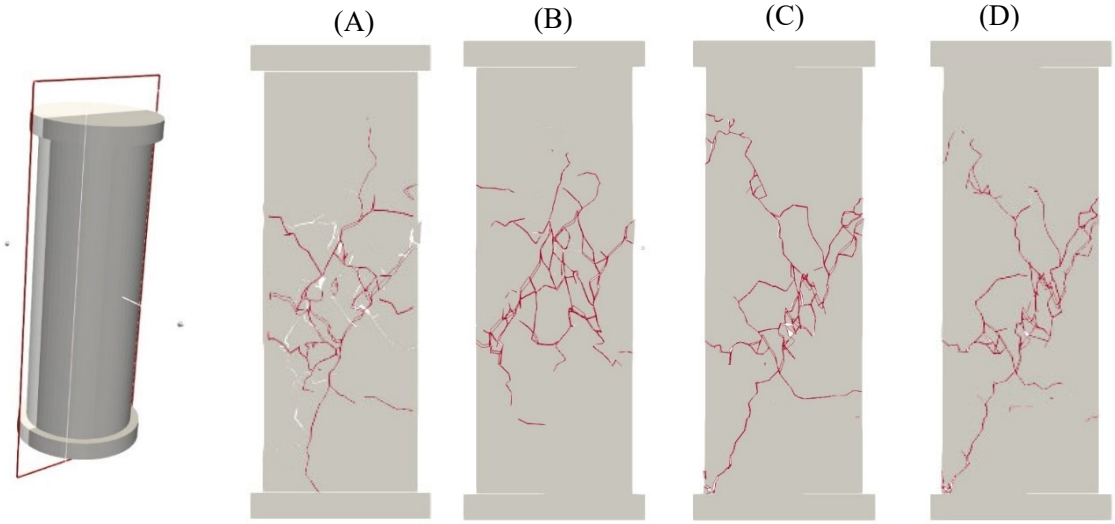

ii) Numerical simulations

Fig. 12. Comparisons between the failure patterns of the sandstones subjected to 0 (A), 20 (B), 40 (C) and 60 (D) freeze-thaw cycles in the UCS tests obtained from i) laboratory experiments and ii) 3D numerical simulations

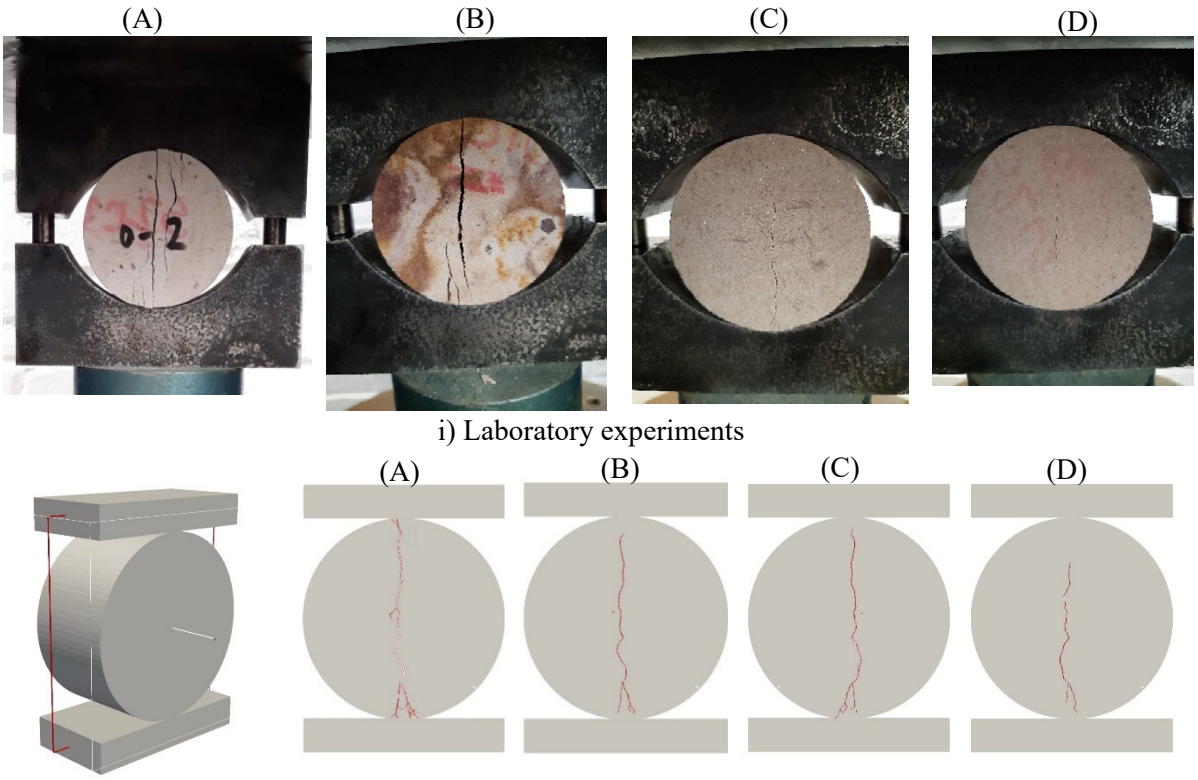

Fig. 13. Comparisons between the failure patterns of the sandstones subjected to 0 (A), 20 (B), 40 (C) and 60 (D) freeze-thaw cycles in the BTS tests obtained from i) laboratory experiments and ii) 3D numerical simulations